

Letter of Intent for PAC34

Deeply Virtual Compton Scattering on the Neutron with CLAS at 12 GeV

M. Battaglieri, R. De Vita, M. Osipenko, M. Ripani,  (INFN Genova)

M. Mirazita, S. Pereira, P. Rossi,... (INFN Frascati)

M. Guidal, M. Mac Cormick, S. Niccolai, S. Pisano,... (IPN Orsay)

A. El Alaoui, E. Voutier,... (LPSC Grenoble)

J. Ball, M. Garcon, S. Procureur, F. Sabatie,... (SPhN-CEA Saclay)

A. D'Angelo,... (Università di Roma 2 - Tor Vergata)

K. Livingstone, ~~e~~, G. Rosner,... (University of Glasgow)

November 25, 2008

Abstract

Here's the abstract

1 Introduction

Generalized Parton Distributions are nowadays the object of an intense effort of research, in the perspective of understanding nucleon structure. They describe the correlations between the longitudinal momentum and transverse spatial position of the partons inside the nucleon, they give access to the contribution of the orbital momentum of the quarks to the nucleon spin, they are sensitive to the correlated $q - \bar{q}$ components, etc... The original articles and general reviews on GPDs and details on the formalism can be found in Refs. [1, 2, 3, 4, 5, 6, 7].

The nucleon GPDs are the structure functions which are accessed in the measurement of the exclusive lepto-production of a photon (or of a meson) on the nucleon, at sufficiently large Q^2 , where Q^2 is the virtuality of the

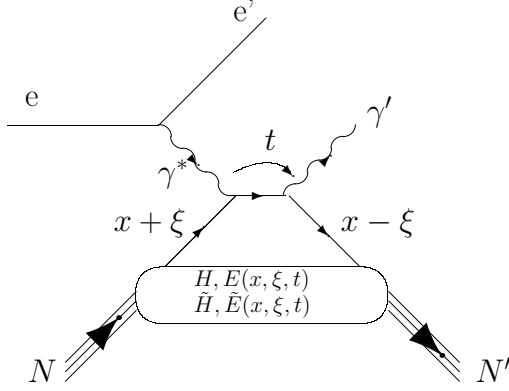


Figure 1: The handbag diagram for the DVCS process on a nucleon $eN \rightarrow e'N'\gamma'$. Here $x + \xi$ and $x - \xi$ are the longitudinal momentum fractions of the initial and final quark, respectively, and $t = (p - p')^2$ is the squared momentum transfer between the initial and final protons (or equivalently between the two photons). There is also a crossed diagram which is not shown here.

photon emitted by the initial lepton. Fig. 1 illustrates such kind of process. Considering only helicity-conserving quantities and the quark sector, there are four GPDs, $H, \tilde{H}, E, \tilde{E}$, which depend, in leading-order and leading-twist QCD, upon three variables: x, ξ and t . $x - \xi$ and $x + \xi$ are the longitudinal momentum fractions of the quarks, respectively, coming out and going back into the nucleon and t is the squared four-momentum transfer between the final and initial nucleon. ☰

~~However~~, an important issue is that among the three variables, x, ξ and t , only two, ξ and t , are accessible experimentally (in the Bjorken limit, $\xi = \frac{x_B/2}{1-x_B/2}$, where x_B is the standard Bjorken variable). Formally, the DVCS amplitude is proportional to:

$$\int_{-1}^{+1} dx \frac{H(\mp x, \xi, t)}{x \pm \xi \mp i\epsilon} + \dots \quad (1)$$


☰ (where the ellipsis stands for similar terms for E, \tilde{H} and \tilde{E}).

Decomposing this expression into its real and an imaginary part, it is found that the maximum information that can be extracted from the experimental data at a given (ξ, t) point is $H(\pm \xi, \xi, t)$ when measuring an observable sensitive to the imaginary part of the DVCS amplitude, and $\int_{-1}^{+1} dx \frac{H(\mp x, \xi, t)}{x \pm \xi}$ ▲ when measuring an observable sensitive to the real part of the DVCS amplitude. Knowing the GPDs at some particular point $(\pm \xi, \xi, t)$ and their

weighted integral over x does not, of course, uniquely define them. Therefore, unavoidably, a model input will be required, to make the interpolation over the x variable.

The DVCS process is accompanied by the Bethe-Heitler (BH) process, in which the final-state photon is radiated by the incoming or scattered electron and not by the nucleon itself. The BH process, which is not sensitive to GPDs, is experimentally indistinguishable from the DVCS and interferes with it, complicating the matter. However, considering that the nucleon form factors are well known at small t , the BH process is precisely calculable theoretically.

It is therefore clearly a highly non-trivial task to actually measure the GPDs. It calls for a long-term experimental program comprising the measurement of different observables: cross sections, beam-, longitudinal and transverse target- single polarization observables, double polarization observables and also possibly beam-charge asymmetries, timelike Compton scattering, etc... Ref. [8] shows the information brought by the various observables.

Such dedicated experimental program, concentrating on a proton target, has started worldwide in these past few years.  JLab has provided the first measurement, in the valence region, of beam-polarized and unpolarized DVCS cross sections, in a limited phase-space domain, with the Hall A collaboration [9], and several beam spin asymmetries (BSA), over a large kinematic range, with the CLAS collaboration [10]. These first data will soon be completed with a series of new experiments aimed to measure accurately longitudinally [11] and transversely [12] polarized target-spin asymmetries and cross sections (along with double-polarization observables) and new precise unpolarized and beam-polarized cross sections at new kinematics [13, 14]. Beam-charge asymmetries, BSAs and transversely-polarized target-spin asymmetries have also been measured by the HERMES collaboration [18].

2 Motivation: neutron GPDs

The aim of this LOI is to start a similar experimental program with a neutron target for which only “pioneering” BSAs, measured on a limited phase-space domain and with various approximations, are available [17].

Measuring neutron GPDs is highly complementary to measuring proton GPDs. Neutron and proton GPDs are independent quantities, like neutron and proton form factors. However, measuring both GPDs allows to carry out a flavor separation. For instance,

$$H^p(\xi, \xi, t) = \frac{4}{9}H^u(\xi, \xi, t) + \frac{1}{9}H^d(\xi, \xi, t), \quad (2)$$

while

$$H^n(\xi, \xi, t) = \frac{1}{9}H^u(\xi, \xi, t) + \frac{4}{9}H^d(\xi, \xi, t) \quad (3)$$

(and similarly for E , \tilde{H} and \tilde{E}).

Also, concerning the BSA, which is the main concern of this LOI, it can be shown that, in the case of DVCS on the neutron, its amplitude is mainly governed by the GPD E , the least known of the GPDs. In particular, E is one of the two GPDs entering Ji's sum rule:

$$J_q = \frac{1}{2} \int_{-1}^{+1} dx x [H^q(x, \xi, t=0) + E^q(x, \xi, t=0)] . \quad (4)$$

It is therefore crucial to obtain some experimental constraints on E in order to make some first steps towards the estimation of the contribution of the orbital momentum of the quarks to the nucleon spin. In order to make a quark-flavor separation, both E^n and E^p are needed: this LOI mainly aims at E^n . E^p can be accessed through transverse-target polarization or double (beam-target) polarization observables on the proton [8], which are, as previously mentioned, the goals of experiments already planned at JLab.

Hereafter, the VGG model [19, 20], which parametrizes GPDs and calculates the associated DVCS observables, has been adopted, in order to confirm and quantify (albeit in a model-dependent way) the sensitivity of the neutron-DVCS BSA to the GPD E . An interesting feature of the VGG model is that the parametrization of the GPD E is dependent on the two parameters J_u and J_d , i.e. the total spin (orbital momentum+intrinsic spin) contributions of the u and d quarks respectively. The idea is that a given shape in x for the GPD E^q is assumed, and then the overall normalization is proportional to J_q (see ref. [5] for more details). Figure 2 shows the BSA for nDVCS as a function of the four independent variables describing the DVCS process, ϕ , $-t$, x_B and Q^2 , for different values of J_u and J_d , as predicted by the VGG model. The central kinematics for Fig. 2 is $E_e=11$ GeV, $x_B=0.17$, $Q^2=2$ GeV², $-t=0.4$ GeV² and $\phi=60^\circ$. Although some the J_u , J_d values are probably unrealistic (for instance $J_d=0.8$, which would imply that 80% of the spin of the proton comes from the d quark), nevertheless, this shows the strong sensitivity of this BSA to E and, in the framework of the VGG model, to J_q . One sees that these BSAs can extend from 10 to 50%, with spectacular changes of sign depending on the relative signs of J_u and J_d , and therefore they can be as large, in magnitude, as the proton-DVCS beam-spin asymmetries that have recently been measured [10]. However, the crucial difference is that these "large" neutron-DVCS asymmetries are obtained only in a specific phase space region, i.e. only around $x_B=0.1$ or 0.15 . To reach such "low" x_B , at sufficiently large Q^2 , an 11-GeV electron beam is needed. The current 6-GeV beam allows to explore mainly the $x_B \approx 0.35$ region where the BSA

is not maximum at all. This is confirmed by the exploratory measurement of the JLab Hall A collaboration [17] where neutron-DVCS BSAs essentially consistent with zero were obtained and for which the J_q sensitivity was therefore minimal.

Figure 2 shows the corresponding BSAs, at approximatively the same kinematics, for the proton case. It is clear that the sensitivity to E or, alternatively to J_u and J_d , is much less. This is mainly due to the fact that the proton-DVCS BSA is mainly sensitive to the H GPD, the weight of the E GPD being suppressed by kinematical factors.

Finally, Fig. 4 shows the comparison of the unpolarized cross section for the proton- and neutron-DVCS cross sections at approximately the same kinematics, as a function of ϕ , $-t$ and x_B , according to the VGG model with $J_u = 0.3$ and $J_d = 0.1$. One sees that the neutron-DVCS cross sections are, depending on the kinematics, a factor 3 to 5 below the proton-DVCS cross sections.

3 Kinematics for nDVCS at 11 GeV

An event generator for DVCS on the neutron inside a deuterium target has been developed [21]. The DVCS amplitude is calculated according to the BKM formalism [22], while the GPDs have been taken from the standard CLAS DVCS generator [23] (MORE PRECISE INFOS NEEDED, WE'LL ASK HARUT). The Fermi-motion distribution is calculated with the Paris potential [24].

Figures 5, 6, and 7 show the coverage in Q^2 , x_B and t that is obtained from the event generator for the nDVCS reaction, with an electron-beam energy of 11 GeV. Cuts simulating the forward-CLAS12 acceptance for the electron ($5^\circ < \theta_e < 35^\circ$ and fiducial cuts on ϕ_e to exclude the dead regions between sectors), as well as kinematic cuts to ensure the applicability of the GPD formalism ($Q^2 > 1 \text{ GeV}^2/c^2$, $t > -1.1 \text{ GeV}^2/c^2$) have been applied.

Figures 8, 9, and 10 show θ as a function of momentum for, respectively, the electron, the photon and the neutron. As expected, the electron and the photon are mostly emitted at forward angles, while the recoil neutron is going at backwards angles.

4 Central Neutron Detector

The minimal requirement in order to ensure the exclusivity of the nDVCS reaction is to fully detect (PID, angles and energy) the scattered electron and the photon, and to at least identify the neutron and measure its angles θ and ϕ . This gives the 8 observables which, together with the 4 constraints coming from momentum and energy

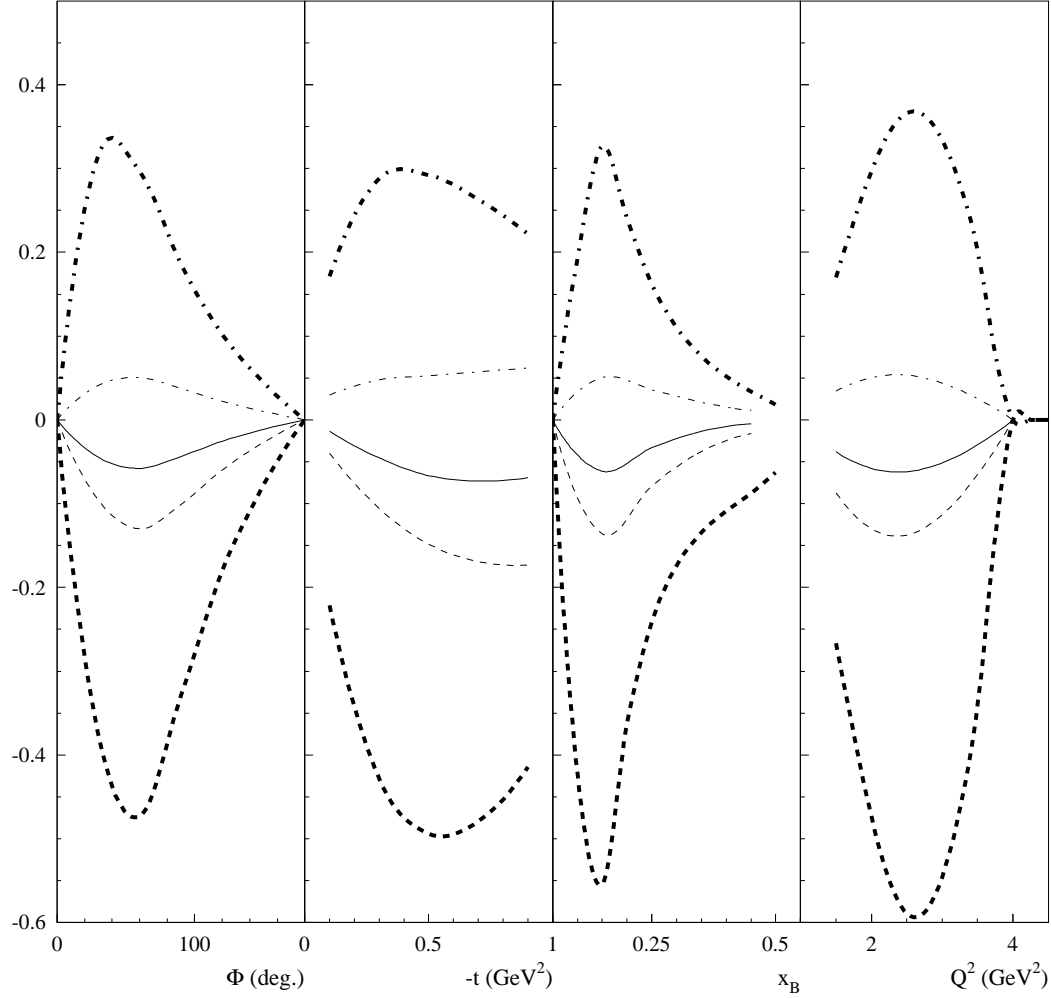


Figure 2: Predicted beam-spin asymmetry for DVCS on a neutron target, plotted as a function of (from left to right) ϕ , $-t$, x_B , and Q^2 . The central kinematics is : $E_e=11$ GeV, $x_B=0.17$, $Q^2=2$ GeV², $-t=0.4$ GeV² and $\phi=60^\circ$. All distributions have been calculated at this central kinematics, except for the variable against which each distribution is plotted. The curves are obtained for different combinations of values of J_u and J_d : ($J_u = 0.3, J_d = 0.1$) -solid curve-, ($J_u = 0.8, J_d = 0.1$) -thin dashed curve-, ($J_u = -0.5, J_d = 0.1$) -thin dash-dotted curve-, ($J_u = 0.3, J_d = 0.8$) -thick dashed curve-, ($J_u = 0.3, J_d = -0.5$) -thick dash-dotted curve.

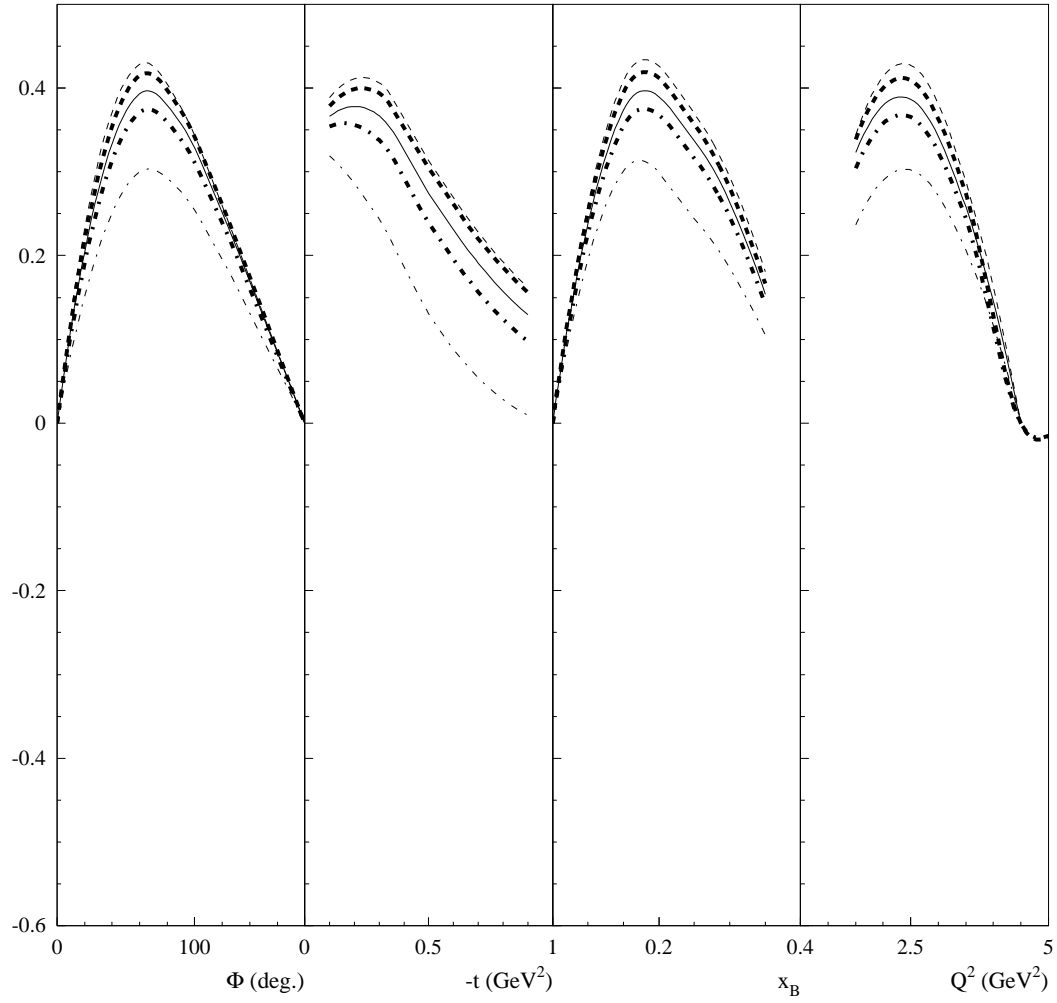


Figure 3: Beam-spin asymmetry for DVCS on a proton target, plotted as a function of (from left to right) ϕ , $-t$, x_B and Q^2 , as predicted by the VGG model. $E_e=11$ GeV, $x_B=0.2$, $Q^2=2$ GeV², $-t=0.2$ GeV² and $\phi=60^\circ$. Otherwise, same conditions and conventions as for Fig. 2.

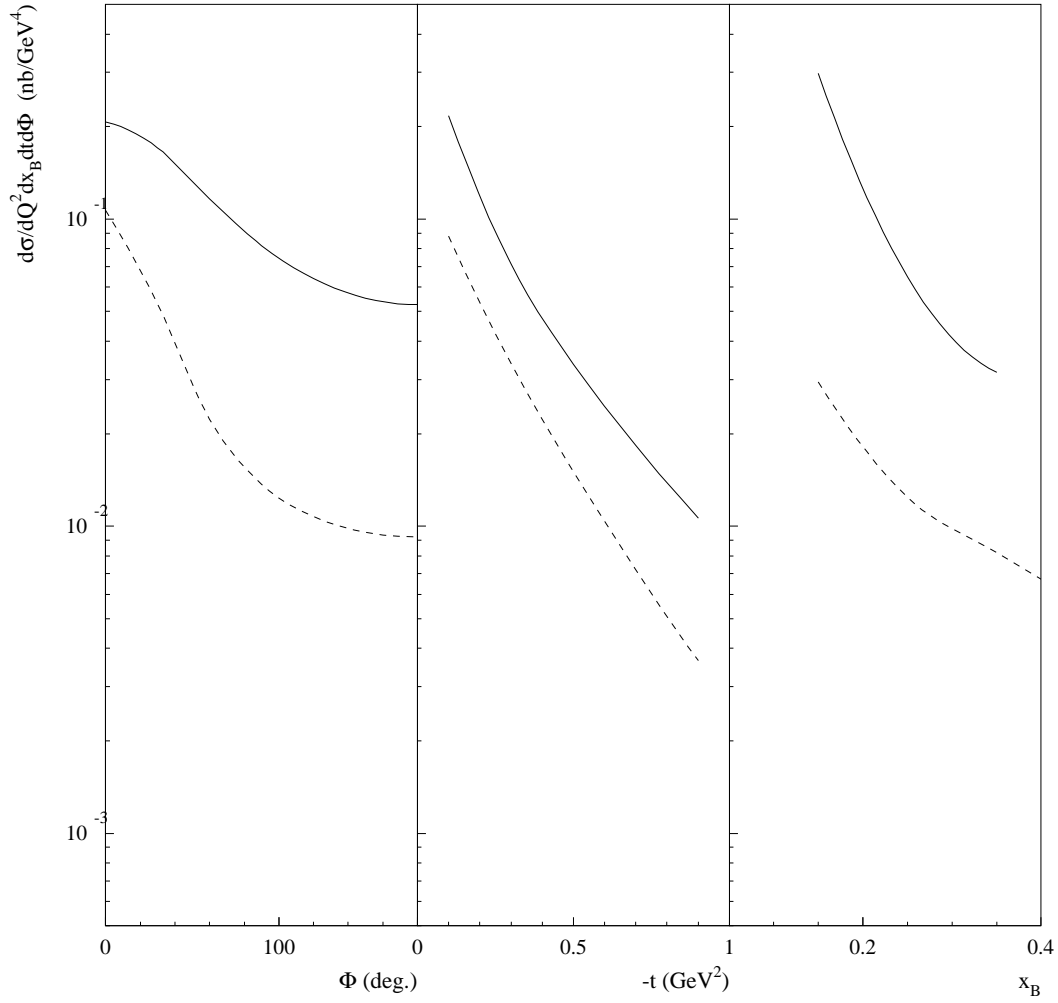


Figure 4: Unpolarized cross section for DVCS on a proton target (solid curves) and for a neutron target (dashed curve), plotted as a function of (from left to right) ϕ , $-t$ and x_B . Same central kinematics as for fig. 3 (for the proton) and fig. 2 (for the neutron).

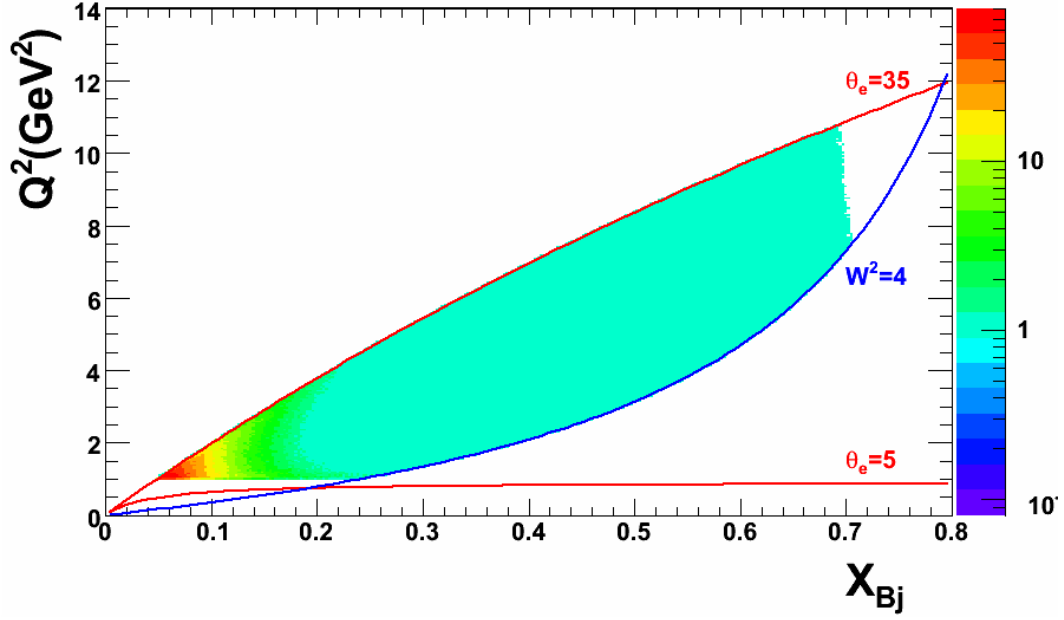


Figure 5: Q^2 as a function of x_B , for nDVCS events. The colored lines represent the cuts applied to the output of the event generator to keep into account the forward-CLAS12 acceptance (cuts on θ_e) and to insure to be out of the region of resonances ($W > 2$).

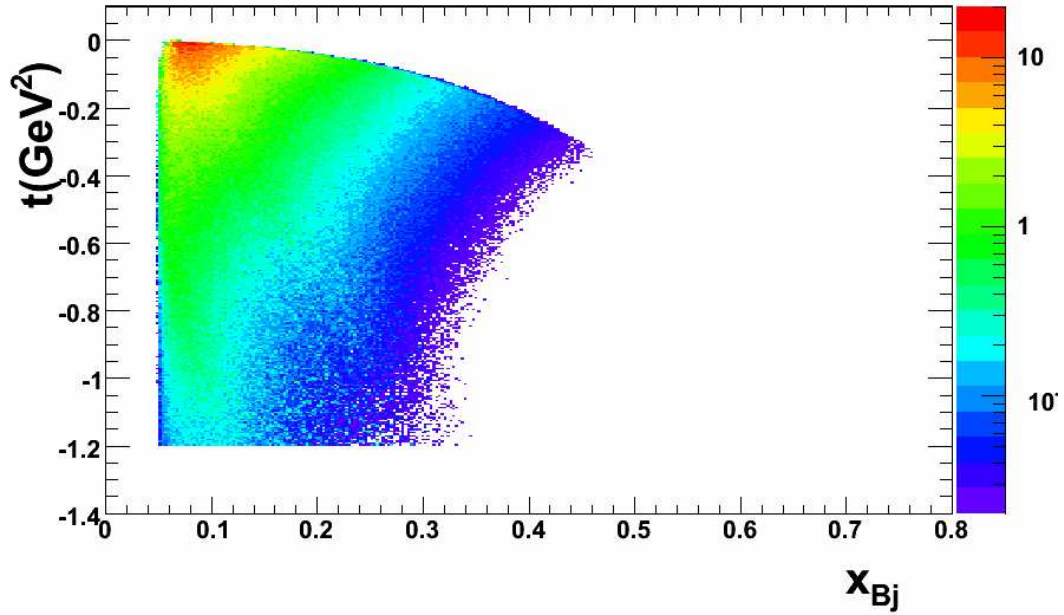


Figure 6: t as a function of x_B , for nDVCS events. Forward-CLAS12 acceptance cuts and physics cuts included.

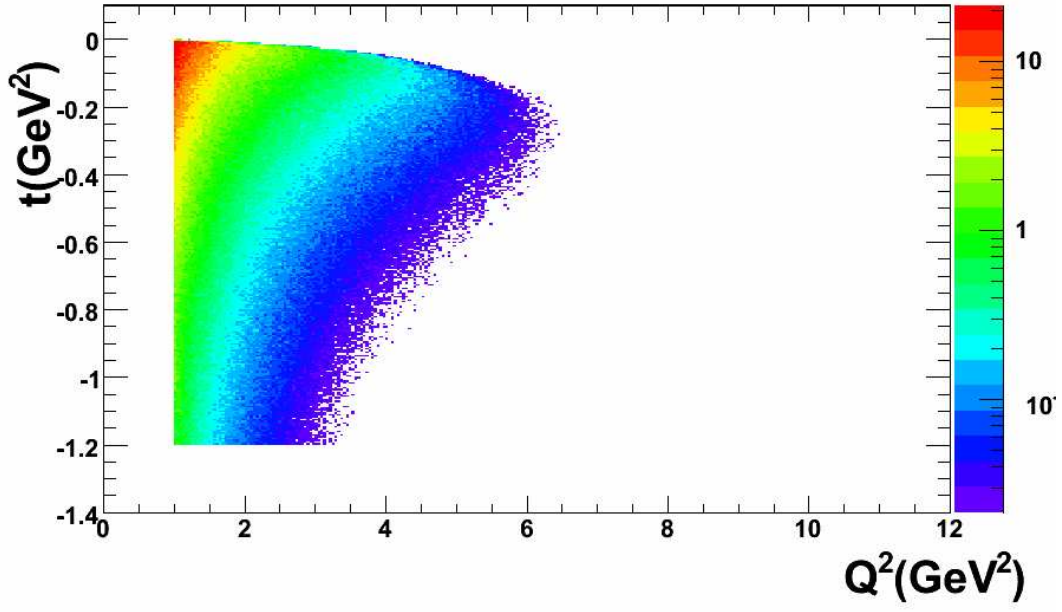


Figure 7: t as a function of Q^2 , for nDVCS events. Forward-CLAS12 acceptance cuts and physics cuts included.

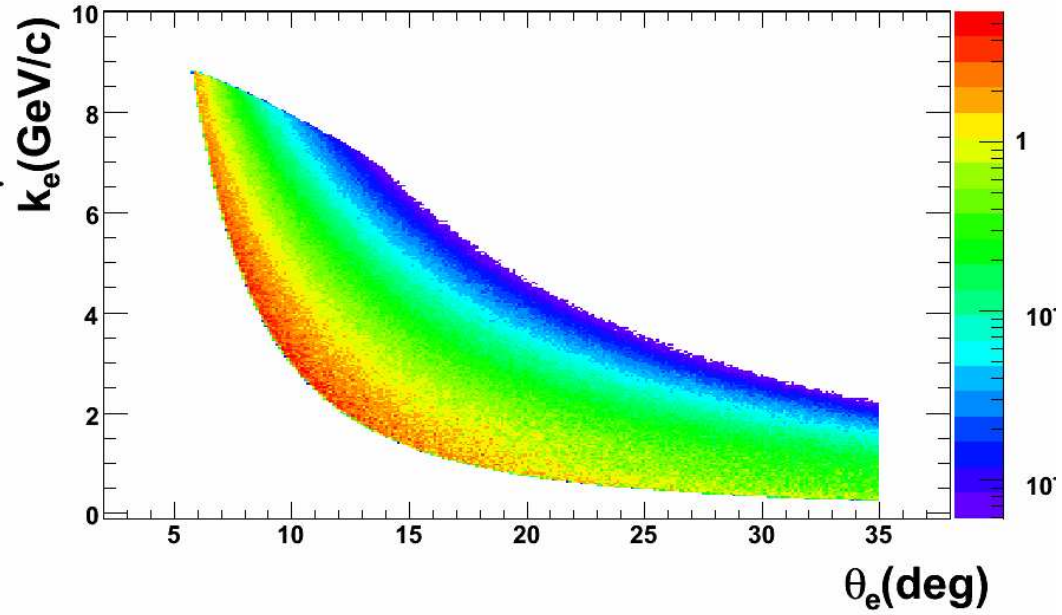


Figure 8: Electron energy as a function of electron polar angle, for nDVCS events. Forward-CLAS12 acceptance cuts and physics cuts included.

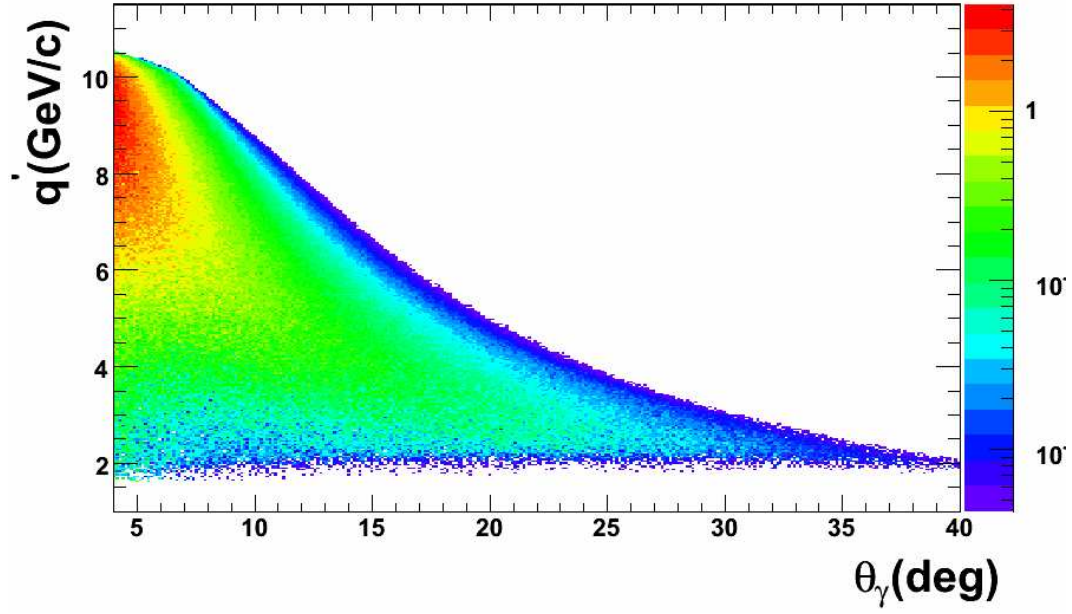


Figure 9: Photon energy as a function of photon polar angle, for nDVCS events. Forward-CLAS12 acceptance cuts and physics cuts included.

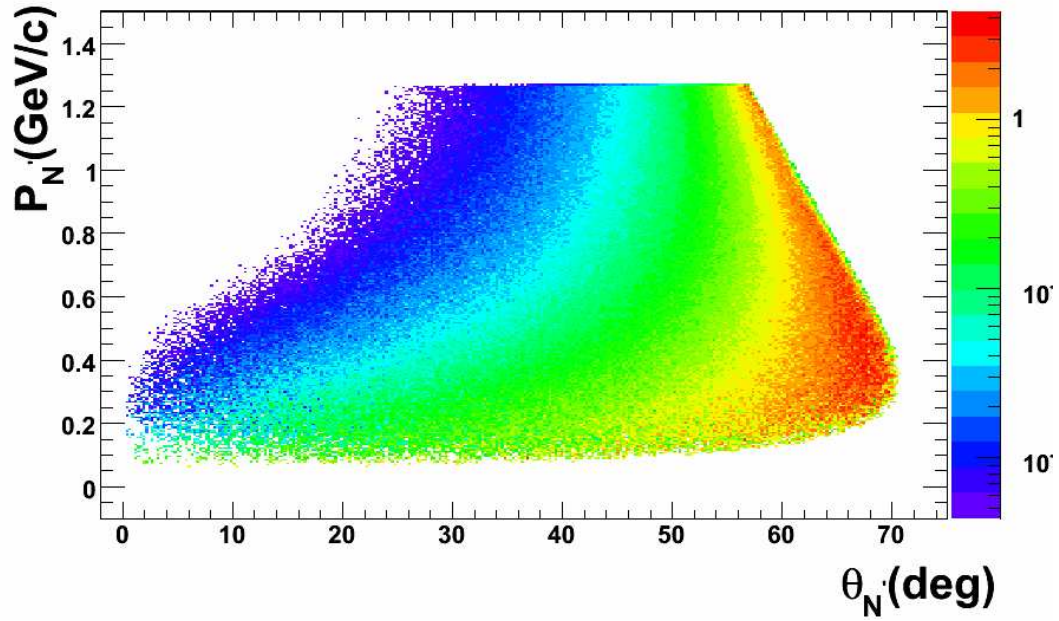


Figure 10: Neutron momentum as a function of neutron polar angle, for nDVCS events. Forward-CLAS12 acceptance cuts and physics cuts included.

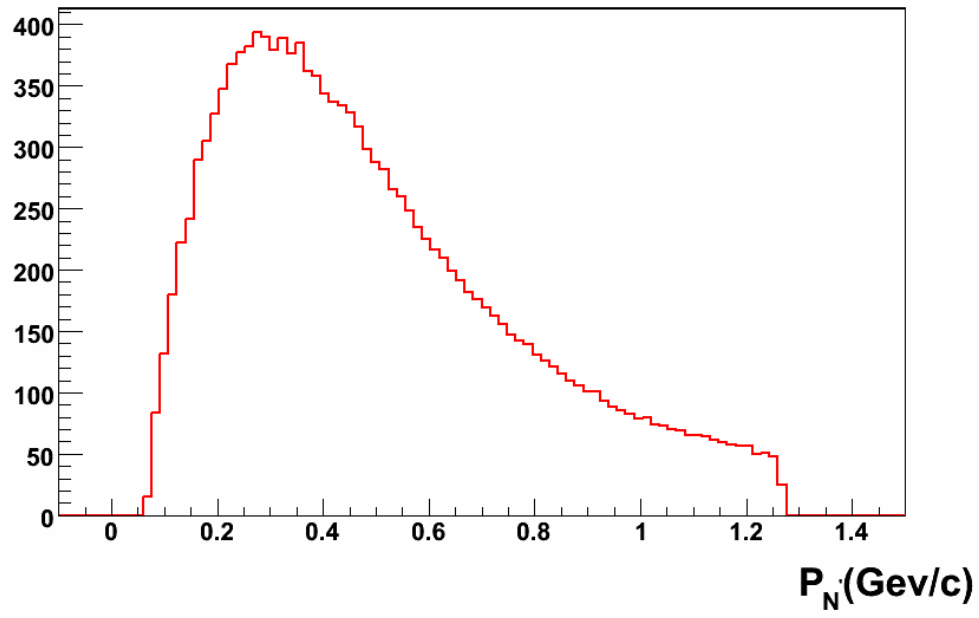


Figure 11: Neutron momentum distribution, for nDVCS events.

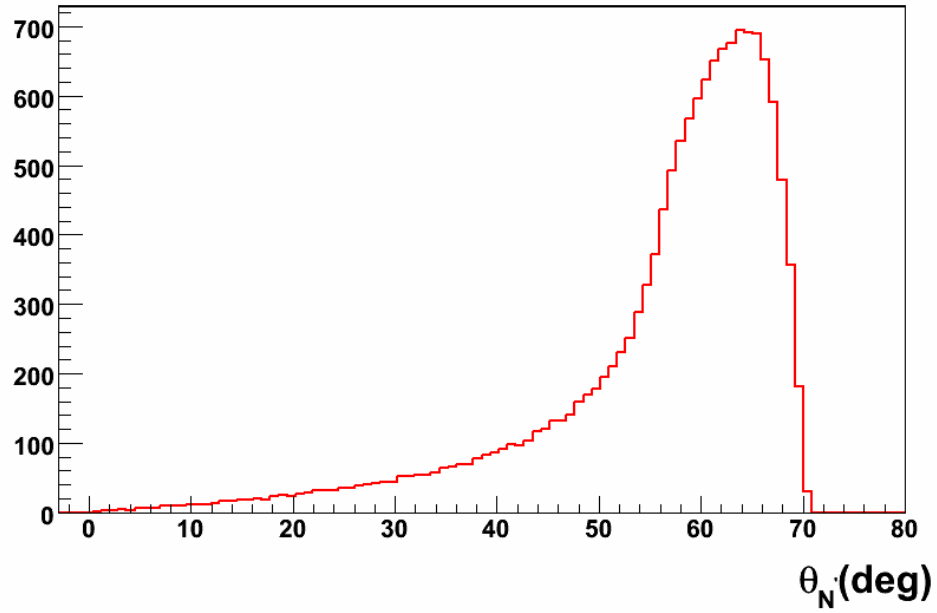


Figure 12: Neutron polar angle, for nDVCS events.

conservation, complete the kinematics (4 particles in the final state \rightarrow 12 unknowns).

As shown in the previous section, the electron and the DVCS photon will be emitted at small angles, and thus will be detected in the forward part of CLAS12, while the neutron will be emitted predominantly (for $\sim 80\%$ of the events) at $\theta > 40^\circ$ in the laboratory frame, with average momentum around 0.4 GeV/c. This points to the necessity to add a neutron detector to the Central Detector of CLAS12.

The available space in the Central Detector is limited by the presence of the CTOF and of the magnet, which leave about 10 cm free (Fig. 13). However, the CTOF can also be used to detect neutrons. The central tracker can also be very useful as a veto for charged particles. Finally, it is important to remind that there will be a surrounding magnetic field of 5 T, which complicates the issue of light collection. This aspect will be addressed in Section 4.4.

After considering various possible solutions, the design for the Central Neutron Detector (CND) that has been retained consists of a barrel of standard plastic scintillator bars (Fig. 14), of trapezoidal shape (Fig. 15), all with their long sides parallel to the beam direction. This geometry mimicks the one of the CTOF. The current plan for the detector segmentation, which can still be modified and optimized, is to have 30 azimuthal segments and 4 in the radial direction, for a total of 120 scintillator bars. Each bar, which is 66 cm long and 2.5 cm thick, will have light readout at each of its two sides.

In order to study the performances of this detector, its geometry has been added to the CLAS12 GEANT4-based simulation package, Gemc [25]. Simulations, which included all the components of the Central Detector, have been run to evaluate the efficiency of the CND for neutrons, its ability to discriminate between neutrons and photons, and its angular resolutions. Neutrons of momenta varying between 0.1 and 1 GeV/c and having polar angle $\theta = 90^\circ$ (corresponding to the “worst-case scenario”, for which the least amount of detector material is traversed and therefore the efficiency is at its lowest) have been generated at fixed azimuthal angle ($\phi = 0^\circ$), pointing to the center of one of the scintillator bars. The results obtained with these simulations are described in the following sections.

4.1 Efficiency

The detection efficiency has been defined as the ratio between the number of events for which the energy deposited in the CND has passed a given threshold and the total number of neutrons generated. Several values of energy threshold, between 0 and 10 MeV, have been tested. Figure 16 shows the efficiency as a function of the threshold, for neutrons with momentum of 0.5 GeV/c. The efficiency, which decreases with increasing threshold, ranges between 16% at the lowest thresholds and 10% at the highest ones. Figure 17 shows instead the efficiency as a function of the momentum of the neutron, at a fixed energy threshold of 5 MeV. The drop at low momenta, below

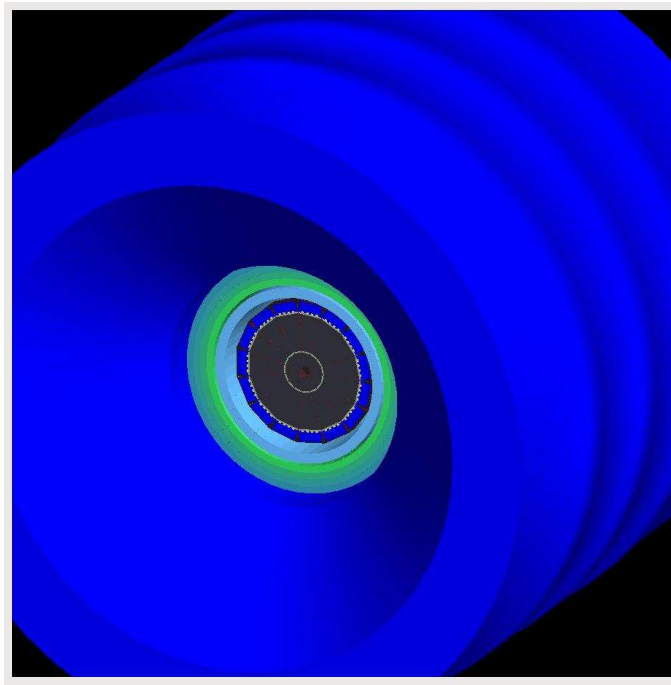


Figure 13: Simulated image of the Central Detector: the light-green/grey area represents the free space between the magnet (dark blue) and the CTOF (light blue).

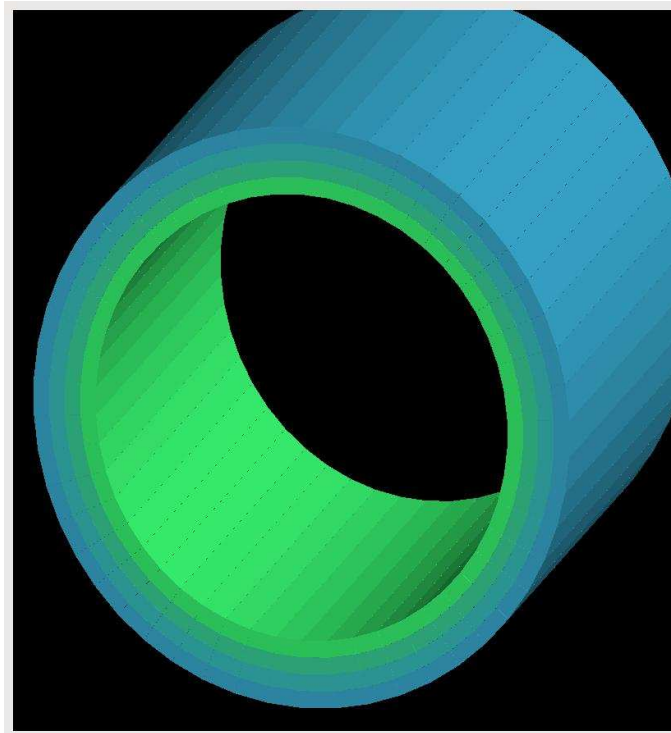


Figure 14: Geometry of the Central Neutron Detector.

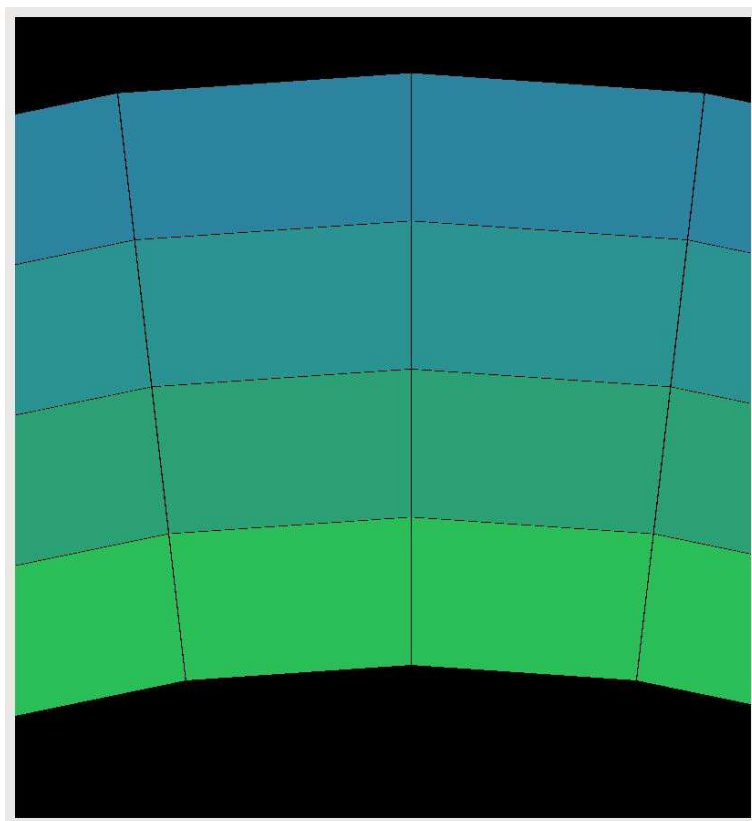


Figure 15: Detail of the geometry of the Central Neutron Detector, showing the trapezoidal shape of the scintillator bars.

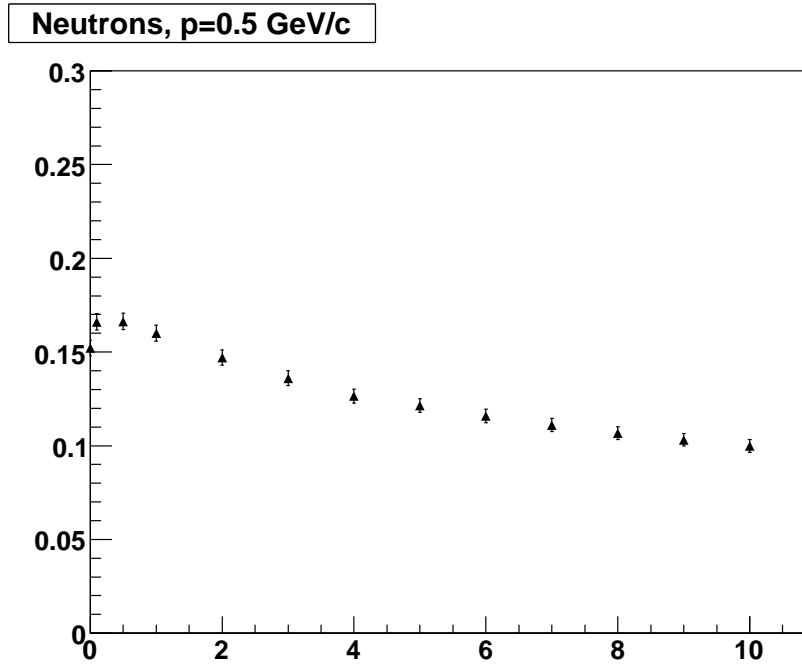


Figure 16: Efficiency for the detection of neutrons having 0.5 GeV/c of momentum, as a function of the threshold on the deposited energy.

0.3 GeV/c, is due to a 5-ns cut on the time-of-flight of the hit. This cut has been applied to suppress the events in which the neutrons interact in the magnet (without depositing energy the CND) and produce secondary particles which then hit the CND, compromising the PID and the determination of the angles. This cut, along with a choice of threshold on the deposited energy of a few MeV (5 is the value chosen at the present stage), is effective in removing these secondary hits (more details on this aspect can be found at [26]).

4.2 Particle Identification

Since the charged particles passing through the CND will be vetoed by the Central Tracker, the only particles that could be mistaken for neutrons in the CND are the photons. Neutrons can be discriminated from photons by means of their β . Therefore, the β distributions that can be obtained with the CND for neutrons and photons have been studied with the aid of the Gemc simulation. After choosing as “good hit” the one for which the first one, within the event, having energy deposition above threshold, β is computed as

$$\beta = \frac{l}{t \cdot c}, \quad (5)$$

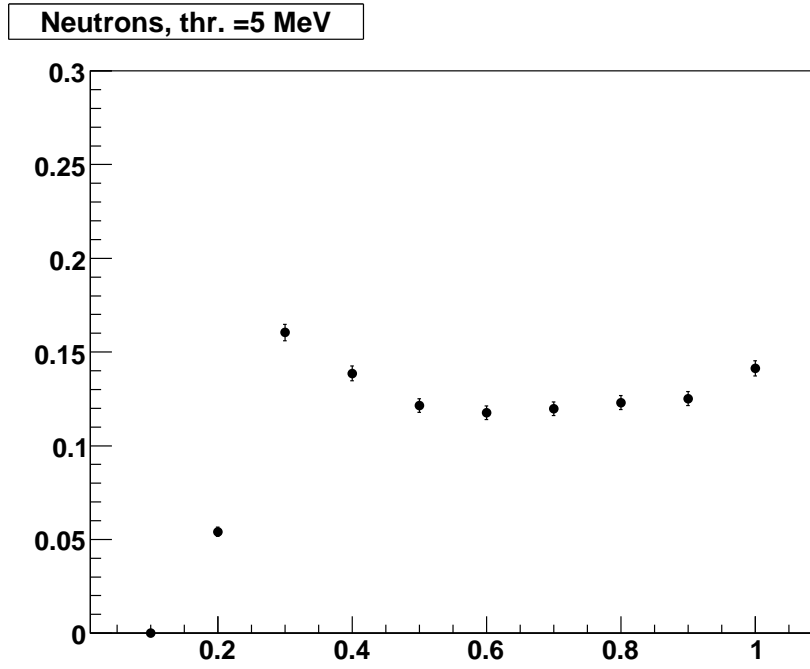


Figure 17: Efficiency for the detection of neutrons, as a function of neutron momentum, for a 5-MeV threshold on the deposited energy.

where

$$l = \sqrt{h^2 + z^2}, \quad (6)$$

$$z = (t_l - t_r) \cdot v_{eff}/2, \quad (7)$$

h is the distance from the vertex to the middle of the layer where the hit took place,

$$t = \frac{1}{2}(t_l + t_r), \quad (8)$$

t_l and t_r are the times measured at the two sides of the scintillator bar, which in the simulation are computed

as

$$t_{l(r)} = t_{hit} + \frac{L/2. - (+)z}{v_{eff}} + t_s, \quad (9)$$

where t_{hit} is the time of the hit (given by GEANT), L is the length of the bar (66 cm), v_{eff} is the effective velocity of the light in the scintillator ($v_{eff} = 16$ cm/ns), and t_s is a smearing factor. In fact, in order to simulate the effects on the TOF resolution of the light propagation in the scintillators and of the intrinsic resolution of the photodetectors, a gaussian smearing has been applied to the time distribution. The width of this smearing is given by:

$$\sigma = \frac{A}{\sqrt{E_{dep}}}, \quad (10)$$

where E_{dep} is in MeV and A in ns·MeV^{-1/2}. The dependence on the inverse square root was deduced by simulations [27]. The value $A = 0.092$ ns·MeV^{-1/2} was determined by rescaling the parametrization obtained by simulations in order to match the resolution measured in recent cosmic-rays measurements with scintillator bars and ordinary PMTs [28]. For the simulation of the CND, the conservative value $A = 0.2$ ns·MeV^{-1/2} has been chosen, in order to account for the worst resolutions that one might obtain using photodetectors that can collect less light than ordinary PMTs (see Section 4.4).

Figure 18 shows the comparison, for each of the 4 radial layers and integrating over the azimuthal angle, between the β distributions obtained for neutrons of various momenta (0.4, 0.6 and 1 GeV/c, in red, blue, and green respectively) and for 1-GeV photons (in black). Neutrons of momentum of 1 GeV/c can be taken as photons, as the two β distributions begin to overlap, while for lower momenta (which correspond to the range of interest for nDVCS) the n/ γ separation is clear. This conclusions depend, of course, from the actual value of the TOF resolution, which here has been assumed to be a bit more than a factor of two worse than what obtained with ordinary PMTs. This needs to be confirmed by a direct measurement of TOF resolution with the chosen photodetectors, and this work is underway (Section 4.4).

4.3 Angular resolutions

The resolution on the polar angle θ of the neutron that can be obtained with the CND is strongly linked to the TOF resolution. The angle θ can be in fact obtained as

$$\theta = (180/\pi) \cdot \arccos\left(\frac{z}{l}\right) \quad (11)$$

where l and z , that were defined, respectively, in Eqs. 6 and 7, both depend on the time measurement. Using the value $A = 0.2$ ns·MeV^{-1/2} for the gaussian smearing on the timing, the θ resolution was studied with Gemc,

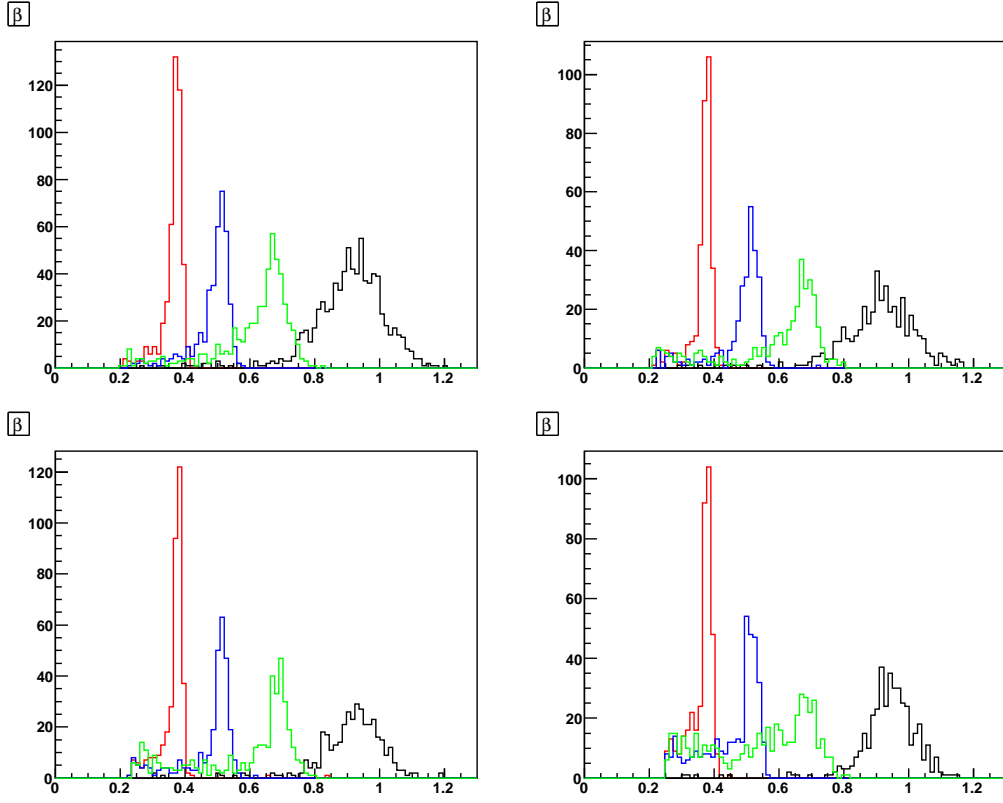


Figure 18: β distributions for neutrons with $p_n = 0.4$ GeV/c (red), neutrons with $p_n = 0.6$ GeV/c (blue), neutrons with $p_n = 1$ GeV/c (green), and photons with $E = 1$ GeV. Each box shows the results for one of the four radial layers that compose the CND (the innermost is on the top left, the outermost is on the bottom right). The threshold on the deposited energy is 5 MeV. The four plots show all hits, integrated over ϕ .

as a function of neutron momentum. The results are shown in Fig. 19, where the mean (top) and the σ of gaussian fits of the θ distribution are plotted as a function of neutron momentum. $\sigma(\theta)$ is constant with the momentum, and roughly equal to 2° . Studies of the θ resolution as a function of θ are underway.

The resolution on the azimuthal angle is directly connected to the total number of scintillator bars along ϕ . In fact, ϕ is given by

$$\phi = \frac{(N_{paddle} - 1) \cdot 360}{N} \quad (12)$$

where N_{paddle} is the ID number of the paddle where the hit took place, and N is the total number of paddles in ϕ (30 at the present stage). The average width of the ϕ distribution for neutrons in the CND, with the current ϕ binning, is $\sigma = 3.5^\circ$ [26]. The choice of the optimal ϕ binning is under study.

The angular resolutions for neutrons obtained with the simulation of the CND will have to be implemented in the nDVCS and $e(p)n\pi^0$ event generators. This will help us to understand at what extent these angular resolutions allow separation between the nDVCS signal and the $e(p)n\pi^0$ background.

4.4 Photodetectors

The two ends of the scintillator bars composing the CND will be located in a high magnetic field (a few T). As the light guides of the CTOF will cover most of the space upstream and downstream, it is necessary to have compact photodetectors that are insensitive to high magnetic fields. These photodetectors must also provide a decent timing resolution (as mentioned in Section 4.2, $\sigma_{TOF} \simeq 120$ ps is needed to discriminate neutrons from photons for neutron momenta up to 1 GeV/c). Currently, three solutions are considered for the light readout of the CND:

- ordinary scintillators read out by a matrix of Silicon Photo Multipliers (SiPM) at each end of each scintillator bar;
- extruded scintillators with one (or more) Wave-Length-Shifting fiber(s) embedded, and a SiPM at each end of the fiber [29];
- ordinary scintillators read out by Micro-Channel PMTs.

The three solutions above are going to be tested with measurements of TOF resolution with cosmic rays. A test-bench has been built for this goal at the IPN Orsay (Fig. 20). It consist of one scintillator bar (BC418) read at one its two sides by the photodetector to be tested and at the other side by an ordinary PMT (in Fig. 20 at both sides are two ordinary (NAME...) PMTs, to make a first reference measurement). In the middle of the bar, above and

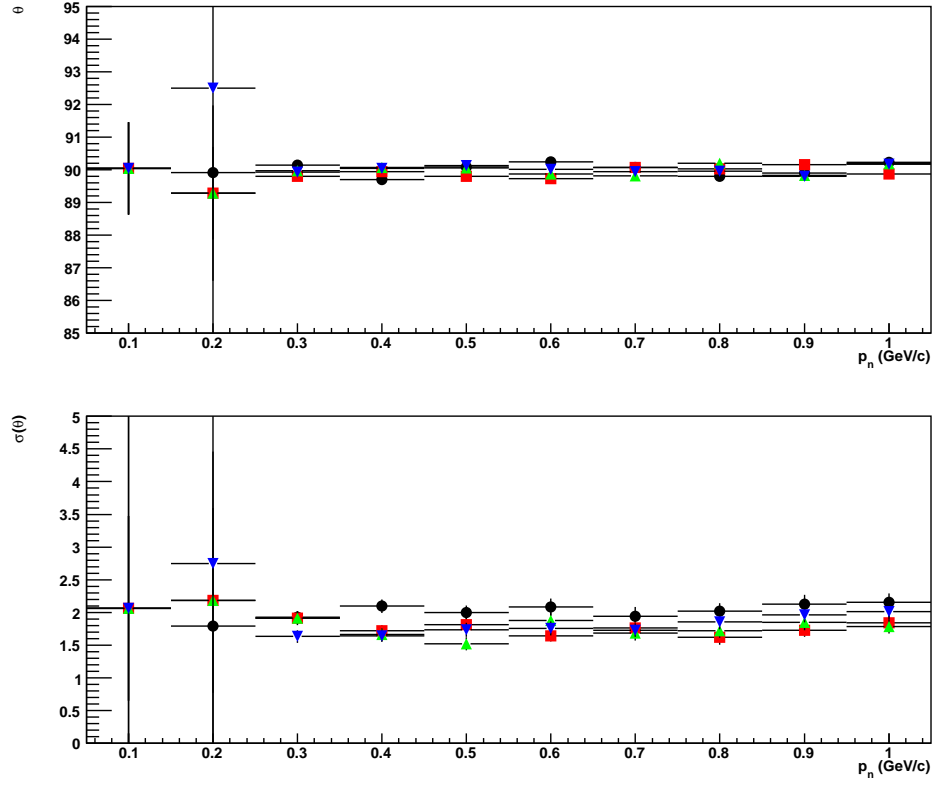


Figure 19: Results of gaussian fits on the θ distributions for neutrons, generated at $\theta = 90^\circ$, for momenta between 0.1 and 1 GeV/c, for a 5-MeV threshold on the deposited energy. Top plot: mean of the θ distribution, as a function of neutron momentum; bottom plot: width (σ) of the θ distribution, as a function of neutron momentum. The four colors of the points correspond to the four radial layers of the CND.

below it are placed two (3!!) smaller (DIMENSIONS!!) scintillators, each read by a fast PMT (NAME...), which will be used to trigger the data acquisition and to insure that the position of the hit is known. The time resolutions of the two left (L) and right (R) photodetectors and of the coincidence between top and bottom scintillators (C) are linked by the following relations:

$$\sigma^2(L/C) = \sigma^2(L - C) = \sigma^2(L) + \sigma^2(C) \quad (13)$$

$$\sigma^2(R/C) = \sigma^2(R - C) = \sigma^2(R) + \sigma^2(C) \quad (14)$$

$$\sigma^2(L/R) = \sigma^2(L - R) = \sigma^2(L) + \sigma^2(R), \quad (15)$$

where $\sigma(L(R)/C)$ stands for the resolution obtained with the left (right) PMT when the trigger came from the top-bottom coincidence, and $\sigma(L/R)$ is the left PMT resolution obtained when triggering on the right one. With three equations and three unknown, the system can be solved and one can deduce $\sigma(L)$, $\sigma(R)$ and $\sigma(C)$.

5 Count-rate estimate

The expected number of reconstructed events for nDVCS has been calculated, as a function of the kinematics, with the event generator described in Section 3. The forward-CLAS12 fiducial cuts have been included, and an overall 10% neutron-detection efficiency has been assumed. The calculation has been done for a luminosity $L = 10^{35} \text{ cm}^{-2}\text{s}^{-1}$ and for 80 days of running time. The number of events, for each 4-dimensional bin (Q^2 , x_B , t and ϕ), has been computed as:

$$N = \frac{d\sigma}{dQ^2 dx_B dt d\phi} \cdot \Delta t \cdot \Delta Q^2 \cdot \Delta x_B \cdot \Delta \phi \cdot L \cdot T \cdot R_{acc} \cdot Eff, \quad (16)$$

where $\frac{d\sigma}{dQ^2 dx_B dt d\phi}$ is the 4-fold differential cross section, T is the running time, L the luminosity, R_{acc} is a bin-by-bin acceptance factor and Eff is the neutron-detection efficiency.

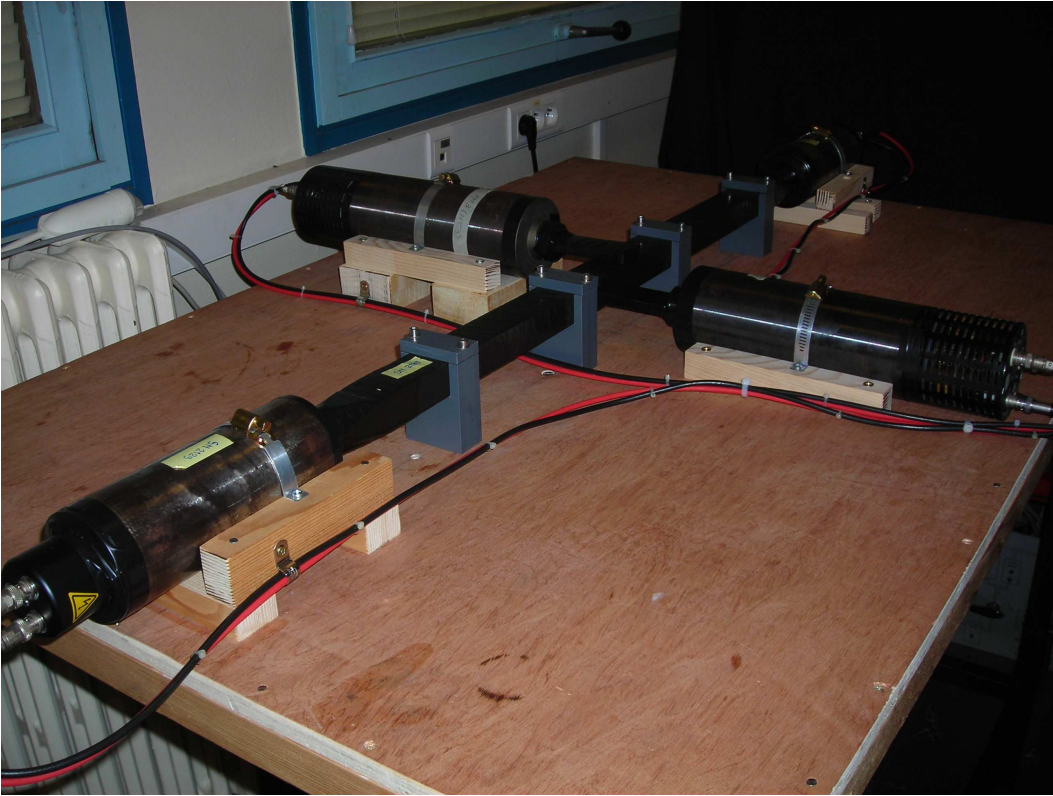


Figure 20: Test bench for the TOF measurement at the IPN Orsay.

In Table 5 the expected 4-fold differential cross sections and corresponding number of events are listed for one particular kinematic bin ($\langle t \rangle = -0.4 \text{ GeV}^2$, $\langle Q^2 \rangle = 2 \text{ GeV}^2$, $x_B = 0.17$) as a function of ϕ . These yields correspond to statistical errors between 3% and 10%. Overall, roughly 1 million of nDVCS events are expected to be collected over the full kinematic range.

6 Backgrounds on the CND

As described above, photons are the main source of background for the CND, as they can be mistaken for neutrons. Charged particles, instead, will be vetoed by the Central Tracker. Two kinds of photons can contribute to this background: physical events, for instance π^0 production where one of the two decay photons is emitted at backwards angles, and photons produced by electromagnetic reactions of the electron beam in the target.

6.1 Physics background

An estimate of the hadronic background has been deduced, using the clasDIS event generator (PYTHIA) REF?. The background events that could mimic a nDVCS event are those having:

Table 1: Expected 4-fold differential cross sections and number of events for nDVCS with CLAS12 and the CND, as a function of ϕ . $\langle t \rangle = -0.4 \text{ GeV}^2$, $\langle Q^2 \rangle = 2 \text{ GeV}^2$, $x_B = 0.17$, $\Delta\phi = 30^\circ$, $\Delta Q^2 = 0.55 \text{ GeV}^2$, $\Delta x_B = 0.05$, $\Delta t = 0.1 \text{ GeV}^2$.

$\phi(^{\circ})$	$\sigma \text{ (nb/GeV}^{-4}\text{)}$	Number of events
7	0.024	1187
27	0.011	1116
58	0.004	387
89	0.00205	204
119	0.0015	147
150	0.00126	125
180	0.0012	119
210	0.00127	126
241	0.00145	147
271	0.0021	205
302	0.0039	386
333	0.0112	1115
353	0.024	1184

- one energetic photon ($E_\gamma > 1 \text{ GeV}$) in forward direction
- one photon in the central detector.

For these kinds of events, the estimated rate at full luminosity ($10^{35} \text{ cm}^{-2}\text{s}^{-1}$) is 2 KHz. If one also requires the missing mass for the $e\gamma$ system (calculated on a neutron target) to be below $1 \text{ GeV}/c^2$, the rate drops to (? RAFFA, HOW MUCH WAS IT?) Hz.

6.2 Electromagnetic background

In order to evaluate the effects of the electromagnetic background on the Central Neutron Detector, in particular to estimate the actual rates seen by the CND due to the background and the energy and timing distributions of the background hits, Gemc simulations have been run in the following conditions [30]: the primary electron has been generated going forward (to simulate the real hadronic event), plus roughly 60000 other electrons have been thrown, distributed in a 124 ns window in bunches 2 ns apart, originating 10 cm upstream the target. These electrons then interact with the target itself, producing an electromagnetic background hitting the neutron detector. 60000 is approximately the number of beam electrons that would pass through the target in a 124 ns time window at the nominal CLAS12 luminosity. 124 ns is the typical time window of the DAQ expected for CLAS12, which corresponds to one event in CLAS12. Figure 21, produced with the interactive version of Gemc, shows one typical “background event” in the Central Detector: the red tracks correspond to negatively charged particles (electrons) while the green ones are neutrals (mostly photons). The hits in the CND, in green/blue-ish, are mainly due to

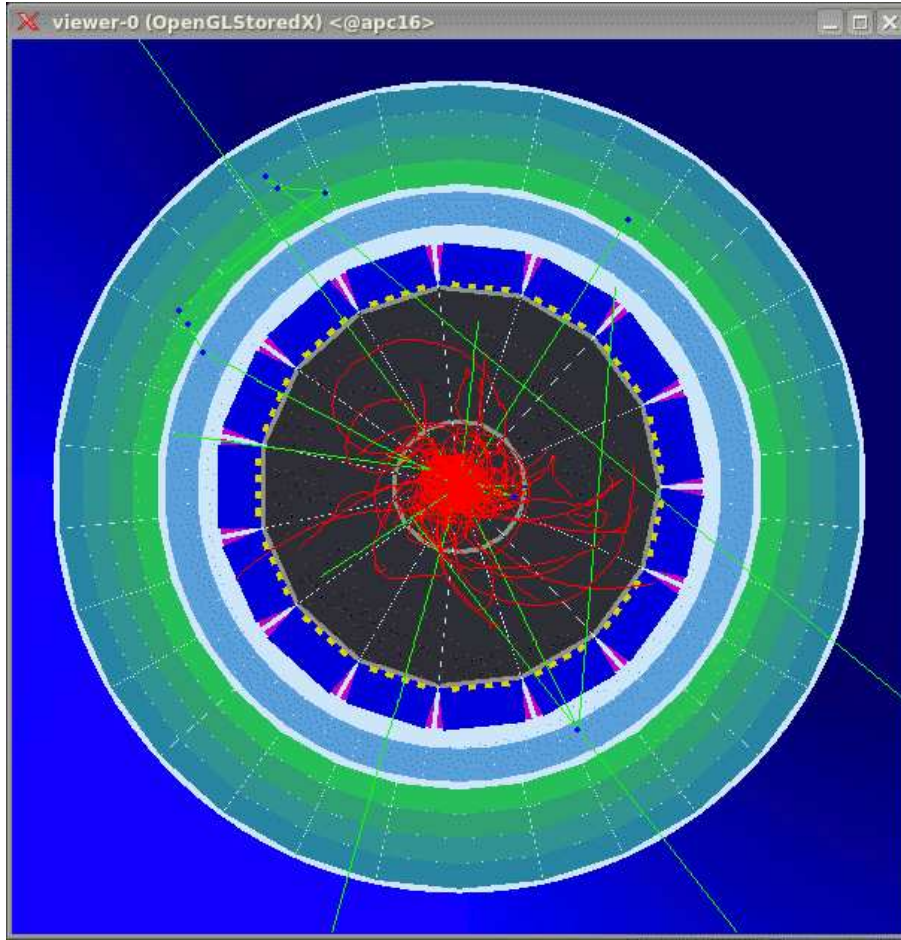


Figure 21: View (from the beam’s perspective) of the Central Detector, for one simulated “background event”. Red tracks correspond to negatively charged particles, green tracks correspond to neutrals. This picture has been obtained for a luminosity $L = 10^{33} \text{ cm}^{-2}\text{s}^{-1}$, corresponding to 1/100 of the nominal luminosity, for practical reasons related to the graphical interface.

photons.

The output of these simulations has been analyzed using the event-reconstruction algorithm adopted to reconstruct neutrons in the CND, for which the chosen hit is the first one depositing energy above a given threshold.

In general, the energy deposited in the CND by the electromagnetic-background photons is quite small, as it can be seen in Figure 22, where the energy deposition in the whole CND is plotted. These photons tend to release their energy mainly in the first radial layers of the CND, as shown in Figure 23. If no threshold on the deposited energy is applied, the total rate on the CND due to the electromagnetic background is 1.95 GHz.

Already applying a 100-KeV threshold on the deposited energy reduces the event rate of the background on the CND to 8 MHz. As it is shown in Fig. 24, roughly 8 hits per event survive, mostly having energy deposit below 1 MeV and with a β distribution peaking at the lowest values of the range ($\beta < 0.1$).

Cutting on the deposited energy at 5 MeV, the value which has been chosen to optimize the PID and angular

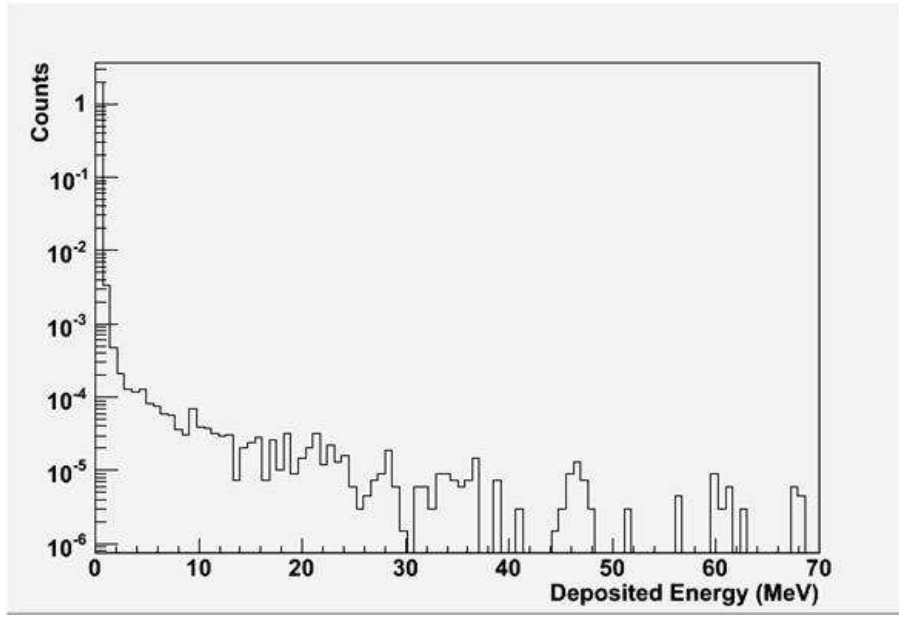


Figure 22: Distribution of the energy deposit in the CND, integrated over all the azimuthal and radial bins, of the hits coming from the generated electromagnetic background. The majority of the events correspond to an energy release below 1 MeV.

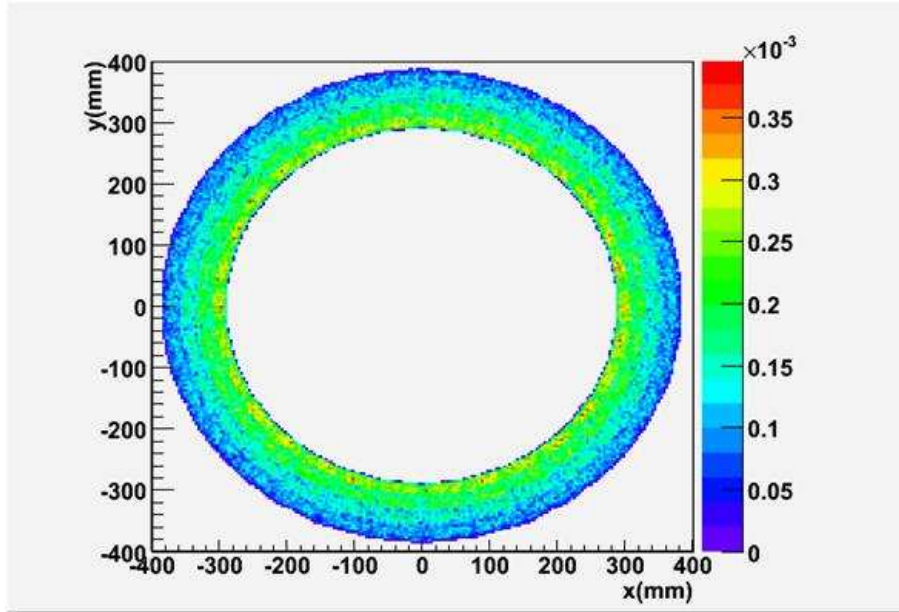


Figure 23: Event distribution for the electromagnetic background in the CND, as a function of the x and y coordinates in the lab frame (z being the beam direction), without any cut on the deposited energy. It can be seen that the majority of the events are concentrated in the innermost layers of the CND.

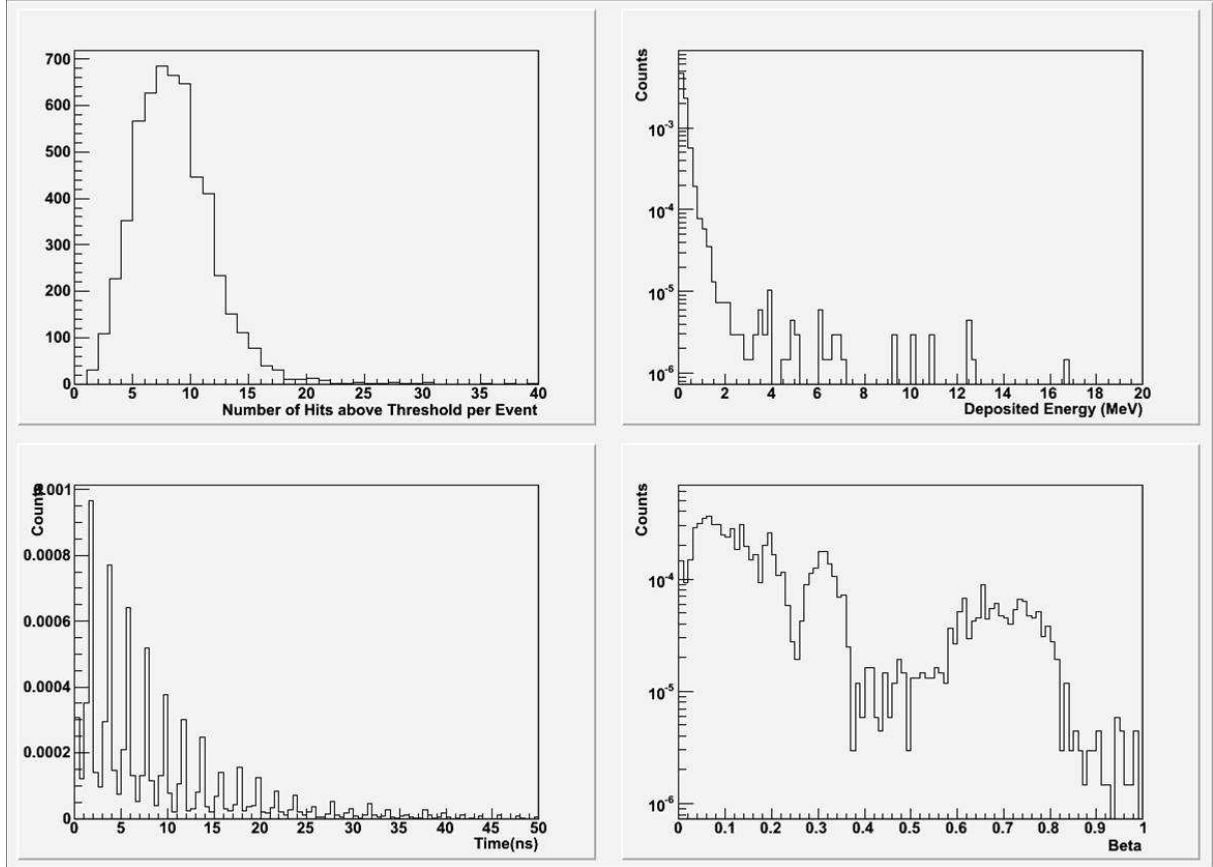


Figure 24: Distributions for the background events surviving to a 100-KeV cut on the energy deposited in the CND. Top left: number of hits above threshold per event. Top right: deposited energy. Bottom right: distribution of the time of the hit (the 2-ns intervals between beam bunches are clearly visible). Bottom left: β distribution.

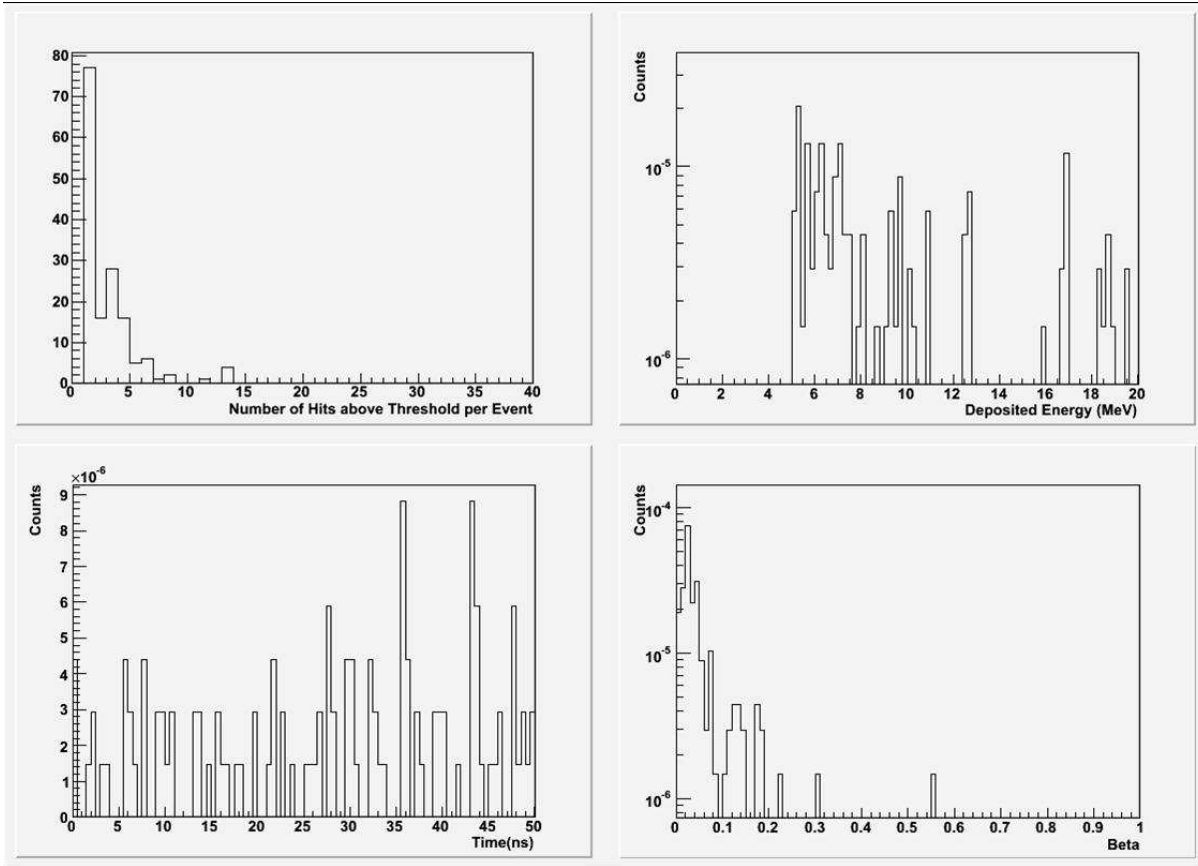


Figure 25: Distributions for the background events surviving to a 5-MeV cut on the energy deposited in the CND. Top left: number of hits above threshold per event. Top right: deposited energy. Bottom right: distribution of the time of the hit. Bottom left: β distribution.

resolution (Section 4.1), the rate drops to 160 KHz. The hit multiplicity per event is roughly 1 (Fig. 25), and almost all of the surviving events have $\beta < 0.1$. Considering that $\beta = 0.1$ corresponds to a neutron momentum of less than $0.1 \text{ GeV}/c^2$, which is below the typical cut that needs to be applied to remove neutron-spectator events (around $0.15 \text{ GeV}/c^2$), the greatest majority of these kinds of background events will be completely removed in the data analysis.

7 Summary and conclusions

References

- [1] D. Müller, D. Robaschik, B. Geyer, F.-M. Dittes, and J. Horejsi, Fortschr. Phys. **42** (1994) 101.
- [2] X. Ji, Phys. Rev. Lett. **78** (1997) 610; Phys. Rev. D **55** (1997) 7114.
- [3] A.V. Radyushkin, Phys. Lett. B **380** (1996) 417; Phys. Rev. D **56** (1997) 5524.

- [4] J.C. Collins, L. Frankfurt and M. Strikman, Phys. Rev. D **56** (1997) 2982.
- [5] K. Goeke, M. V. Polyakov and M. Vanderhaeghen, Prog. Part. Nucl. Phys. **47** (2001) 401.
- [6] M. Diehl, Phys. Rept. **388** (2003) 41.
- [7] A.V. Belitsky, A.V. Radyushkin, Phys. Rept. **418** (2005) 1.
- [8] M. Guidal, Eur. Phys. J. A **37** (2008) 319.
- [9] C. Muñoz Camacho et al., Phys. Rev. Lett. **97**, 262002 (2006).
- [10] F.-X. Girod et al., Phys. Rev. Lett. **100**, 162002 (2008).
- [11] JLab approved experiment E-05-114: “Deeply Virtual Compton Scattering at 6 GeV with polarized target and polarized beam using the CLAS detector”; spokespersons: A. Biselli, L. Elhouadrhiri, K. Joo and S. Niccolai.
- [12] JLab (conditionally) approved experiment E-08-021: “Deeply Virtual Compton Scattering at 6 GeV with transversely polarized target using the CLAS detector”; spokespersons: H. Avakian, V. Burkert, M. Guidal, R. Kaiser and F. Sabatié.
- [13] JLab approved experiment E-06-003: “Deeply Virtual Compton Scattering with CLAS at 6 GeV”; spokespersons: V. Burkert, L. Elhouadrhiri, M. Garçon, R. Niyazov and S. Stepanyan.
- [14] JLab approved experiment E-07-007: “Complete separation of Deeply Virtual Photon and π^0 electroproduction observables of unpolarized protons”; spokespersons: C. Munoz Camacho, J. Roche, C. Hyde-Wright and P.-Y. Bertin.
- [15] JLab approved experiment E-12-06-114: “Measurements of Electron-Helicity Dependent Cross Sections of Deeply Virtual Compton Scattering with CEBAF at 12 GeV”, spokespersons: C. Hyde-Wright, B. Michel, C. Munoz Camacho and J. Roche.
- [16] JLab approved experiment E-12-06-119: “Deeply Virtual Compton Scattering with CLAS at 11 GeV”, spokespersons: V. Burkert, L. Elouadrhiri, M. Garçon, M. Holtrop, D. Ireland, K. Joo, W. Kim, F. Sabatié.
- [17] M. Mazouz et al., Phys. Rev. Lett. **99**, 242501 (2007).
- [18] A. Airapetian et al, arXiv:0802.2499.
- [19] M. Vanderhaeghen, P.A.M. Guichon, M. Guidal, Phys. Rev. D **60**, 094017 (1999).
- [20] M. Guidal, M. V. Polyakov, A. V. Radyushkin and M. Vanderhaeghen, Phys. Rev. D **72**, 054013 (2005).
- [21] A. El Aloui and E. Voutier, private communication.

- [22] A.V. Belitsky, D. Müller, A. Kirchner, Nucl. Phys. B **629** (2002) 323-392.
- [23] H. Avakyan, private communication.
- [24] M. Lacombe et al., Phys. Rev C **21** (1980) 861.
- [25] M. Ungaro, private communication.
- [26] S. Niccolai, [http://clasweb.jlab.org/rungroups/e1-dvcs/wiki/index.php/CLAS12_neutron_detector:update on simulation](http://clasweb.jlab.org/rungroups/e1-dvcs/wiki/index.php/CLAS12_neutron_detector:update_on_simulation) (September 2008).
- [27] M. Mirazita and R. De Vita, private communication.
- [28] S. Koutsnezov, private communication.
- [29] S. Stepanyan, private communication (THERE MUST BE A CLAS-NOTE...).
- [30] R. De Vita, <http://www.jlab.org/devita/bgonly.ppt>